Materials Advances

ROYAL SOCIETY OF CHEMISTRY

PAPER

View Article Online
View Journal | View Issue

Cite this: *Mater. Adv.*, 2024, 5, 7327

Soft, ternary, X- and gamma-ray shielding materials: paraffin-based iron-encapsulated carbon nanotube nanocomposites†

Jolanta Sobczak,[a] Adrian Truszkiewicz,[b] Krzysztof Cwynar,[c] Szymon Ruczka,[de] Anna Kolanowska,[cd] Rafał G. Jędrysiak,[de] Sylwia Waśkiewicz,[f] Marzena Dzida,[c] Sławomir Boncel *[de] and Gaweł Żyła *[g]

Received 4th April 2024,
Accepted 20th July 2024

DOI: 10.1039/d4ma00359d

rsc.li/materials-advances

In the field of radiological protection, there is a growing interest in nano- and microcomposites due to their unique physicochemical properties, flexibility in the component selection (the base ingredient as well as the fillers), and lower toxicity in comparison to the lead (Pb)-based ones. In this study, we manufactured paraffin-based composites with different concentrations of iron-encapsulated multi-walled carbon nanotubes (Fe@MWCNTs) (10 and 20 wt%), which were prone to shape change at average room temperature. Long Fe@MWCNT arrays were synthesized by catalytic chemical vapor deposition (c-CVD) using a saturated (at 293.15 K) toluene solution of ferrocene ($FeCp_2$) (9.6 wt%) as a feedstock toward the highest efficiency for a complete Fe-encapsulation. The experimental data indicate that the shielding properties against gamma- and X-ray radiation are influenced by the filler concentration – the higher CNT content resulted in a greater ability to attenuate incident ionizing radiation. Finally, Fe@MWCNT–paraffin composites demonstrated corrosion resistance, as they did not react with 1 M aqueous solutions of NaCl, NaOH, and HCl.

1 Introduction

Nanotechnology is a rapidly evolving and advancing area that concerns small particles, offering a wide range of research applications, and improvements across various fields. As multi-disciplinary in nature, it encompasses among others chemistry, physics, and materials science to design and fabricate unique materials with superior properties over the existing solutions. One of such area is a broadly understood protection against ionizing radiation. This is due to the wide utilization of radiation in various fields;[1] focusing on gamma radiation and X-rays, they are applied in medicine,[2,3] science,[4–6] and industry,[7,8] to name just a few. Fig. 1 summarizes the most common utilization of gamma- and X-rays in various areas. Furthermore, it is important not to overlook the fact that this holds a particular significance nowadays, in times of energy crisis, where emphasis is placed on the emission-free energy. On the one hand, the most prospective solutions should meet the energy requirements and, on the other hand, be in symbiosis with the ecosystem.[9]

Nevertheless, traditional X-ray and gamma-ray shielding materials rely on utilizing materials with high density, mainly lead (Pb), which is a serious threat to humans health.[10] It is also worth mentioning the presence of other drawbacks such as weight, impracticality, difficult recyclability, and limited accessibility or ability to be produced in desired shapes.[11,12] In order to overcome these limitations and achieve desirable physicochemical properties in addition to the maximum radiation dose suppression, numerous efforts have been made to enhance conventional solutions through the introduction of nano- and microcomposites. Nano- and microcomposites, as a relatively-new class of materials, due to their wide range of choice concerning the main ingredient (the continuous phase), fillers (nano- and micropowders), and other additives (*e.g.* plasticizers),[1,13] gain an

[a] *Doctoral School of the Rzeszów University of Technology, Rzeszów University of Technology, Powstańców Warszawy 12, 35-959 Rzeszów, Poland*
[b] *Department of Photomedicine and Physical Chemistry, Medical College of University of Rzeszów, University of Rzeszów, Warzywna 1A Street, 35-310 Rzeszów, Poland*
[c] *Institute of Chemistry, University of Silesia in Katowice, Szkolna 9, 40-006 Katowice, Poland*
[d] *Department of Organic Chemistry, Bioorganic Chemistry and Biotechnology, Silesian University of Technology, Krzywoustego 4, 44-100 Gliwice, Poland. E-mail: Slawomir.Boncel@polsl.pl*
[e] *Centre for Organic and Nanohybrid Electronics (CONE), Silesian University of Technology, Konarskiego 22B, 44-100 Gliwice, Poland*
[f] *Department of Physical Chemistry and Technology of Polymers, Silesian University of Technology, ks. Marcina Strzody 9, 44-100 Gliwice, Poland*
[g] *Department of Physics and Medical Engineering, Rzeszów University of Technology, Powstańców Warszawy 6, 35-959 Rzeszów, Poland. E-mail: gzyla@prz.edu.pl*

† Electronic supplementary information (ESI) available. See DOI: https://doi.org/10.1039/d4ma00359d

Fig. 1 The most common applications of gamma and X radiation showed as a simplified scheme, which confirms the versatility of the utilization of these types of radiation in various areas including science, medicine and industry as the main ones. Adapted with permission from ref. 1, under RightsLink license number 5751940607057.

advantage over the current (*i.e.* frequently outdated) solutions, as the choice of matrix (with eventual modifier agents) and filler compounds is specifically selected for a clearly-determined application. The compound selection is usually established keeping in mind factors such as: emitted energy level, determination in terms of fixed/movable destination, elimination of a secondary radiation and durability to destructive ionizing radiation effects to mention a few fundamental ones. Having such knowledge, the selection of particles (bearing in mind the morphology in terms of size, type, specific surface area, purity, presence of surface modification, *etc.*) along with main compound guarantee meeting the physicochemical property expectations of such a developed shield. And so, Li *et al.*[14] developed composites based on natural leather with coimpregnated Bi_2O_3 and La_2O_3 nanoparticles to accomplish a lightweight, flexible, and wearable X-ray shield, where minimization of secondary radiation was realized by the additional Bi_2O_3 coating at the bottom. As another example, Tekin *et al.*[15] verified theoretically (using Monte Carlo simulation) the size influence of tungsten oxide (WO_3) particles on the shielding properties of a conventional shield – concrete. A similar study was developed in ref. 16 where the topic of filler size was analyzed on ilmenite–limonite (ILC) concretes filled with WO_3 and PbO particles (50 μm and 50 nm defined diameters) using a simulation approach. Finally, a study where the developed nanocomposite included more than one added filler (for instance boron nitride and graphene nanosheets in the polyester matrix[17]) could also be found. One should not forget that the utilized matrices sometimes are recycled ones, which proves that the scientific world bears in mind the problem of continuously growing waste amounts and remains on alert to partially prevent environmental pollution.[18–21] More importantly, the inclusion of nano- and microparticles in the composition not only reduces the amount of raw materials but also allows for choosing the elements which are safe for the human body, exhibiting low toxicity and mutagenicity, among other factors.[22,23]

Focusing on the fillers, among nano-sized materials carbon nanotubes (CNTs) deserve special attention due to their light weight, high specific surface area, and excellent mechanical, thermal and electrical properties, accompanied by corrosion and oxidation resistance.[24–26] Their particular properties depend on their morphology: diameter, length, shape (*e.g.* straight, waved, coiled, and branched[27]), the number of rolled-up graphene

sheets (multi-walled or single-walled, MWCNTs or SWCNTs), as well as the presence of additions on their surface (covalent and non-covalent functionalization).[28,29] Their potential use in the design of protective materials against X and gamma radiation has already been noticed, as a review paper[30] reports, and included as a component of shielding materials. Remaining in the shielding field, one should not forget utilization of carbon nanotubes as microwave absorbers and electromagnetic interference (EMI) shields.[24,31–33]

Verma *et al.*[34] developed an X-ray shielding nanocomposite, where bismuth(III) oxide (Bi_2O_3) were incorporated on MWCNTs (20–25-μm-long) and along with proper additions resulted in a material in the form of a gel, which was then spread on previously washed, and mechanically rubbed cotton fabric. The shielding bandages had the following dimensions: 60 cm in length, 10 cm in width, and 5 mm in thickness, and were examined on a Nomex Multimeter from PTW with X-ray photons of 50–80 kVp energies, for 200 ms at 100 mA. The study involved three varying bandage samples: untreated bandage, bandage treated only with MWCNTs, and one combining Bi_2O_3 and MWCNTs. The highest X-ray absorption was recorded for the third bandage sample, so the study was extended to verify the effect of the Bi_2O_3 nanoparticles' concentration (70, 75, and 80 wt%) on the shielding properties. Clearly, the results indicated that the higher content of Bi_2O_3 nanoparticles improved the X-ray shielding properties. In another study,[35] the X-ray attenuation efficiency of SWCNTs, MWCNTs, single-wall carbon nanohorns (SWCNHs), fullerene (C_{60}), graphene oxide (GO), and a fabric-textile with a MWCNTs addition was developed, and compared to the highly oriented pyrolytic graphite (HOPG). The sample textile was manufactured with polyester fibers (0.19 mm in thickness) with 8 wt% of MWCNTs containing 2.5 wt% of TiO_2. The disc-shaped samples (apart from HOPG), 13 mm in diameter, were examined using a monochromatic incident X-ray beam of MoK_α (λ_0 = 0.7107 Å) at 50 kV, and 10 mA (and 300 mA for the thickness-dependence study). Considering the mass attenuation coefficient (μ_m) values, the X-ray attenuating ability (50 kV, 10 mA) of the SWCNTs, MWCNTs, SWCNHs, and the fabric-textile with MWCNTs addition were superior in comparison to HOPG. The investigation also included the dependence of the X-ray attenuation ratio on the thickness of the textile sample. It was shown that the attenuation efficiency increased with the thickness, *i.e.*, for a thickness of 24 mm, the attenuation was higher than 70%. Altarawneh *et al.*[36] proposed a mixture composed of gelatin (gelatin from bovine skin type B) and distilled water as a matrix for MWCNTs (with 10–20 μm length and outer diameter 30–50 nm), or activated carbon, which were added in various concentrations: 0, 5, and 10 wt%. The mass attenuation coefficients of the synthesized samples were determined using a cesium source (^{137}Cs, 662 keV energy) along with a sodium iodide (NaI) detector, where the experimental data was collected for 90 min, and compared to the theoretical values predicted by the XCOM program (at energies 1 keV–100 GeV). The authors demonstrated that samples with the MWCNTs addition attenuated slightly more efficiently than those with activated carbon: for 5 wt% addition, the experimentally-designated mass attenuation coefficient values were found as 0.079 ± 0.001 and 0.082 ± 0.001 $cm^2\ g^{-1}$ for activated carbon and MWCNTs, respectively. Overall, the authors recommended using MWCNTs as the addition to shielding composites in the X-ray energy range (rather than in the gamma range) as the stronger interaction appeared when the wavelength of the radiation was near to the interlayer spacing of MWCNTs. The shielding performance of CNT films using ^{241}Am (59.5 keV) and ^{137}Cs (661.7 keV) was also determined.[37] The CNTs contained 3–8 tube walls with declared 7.8 nm average diameter. The CNT films were synthesized using a floating catalyst chemical vapor deposition growth technique, and one layer of this film was about 10-μm-thick. The investigation involved an analysis of a random film, aligned film (15% stretching ratio), and resin-impregnated film (with added 35 wt% epoxy resin) with various numbers of layers: 150, 300, 450, and 600. Considering 59.5 keV energy (for the ^{241}Am source), the highest mass attenuation coefficient was found for the second sample, *i.e.*, the aligned film, and it was 0.6707 $cm^2\ g^{-1}$, while for the random one and resin-impregnated film, the corresponding values were equal to 0.5894, and 0.3051 $cm^2\ g^{-1}$, respectively. Those values were compared to the ones for aluminum, iron, copper, and lead. Considering the beam energy of 661.7 keV, the mass attenuation coefficient was higher for the random and aligned film than for aluminum, iron, and copper. Furthermore, Huang *et al.*[38] manufactured silicone foams with various contents of oxidized MWCNTs (o-MWCNTs): 1, 5, 10, 20, and 30 wt% using solution casting, foaming and cross-linking reactions, in order to verify their gamma radiation stability. The thickness of composites varied from 0.5 to 6.4 mm. The composites were placed into a glass tube and exposed to the ^{60}Co source radiation with the doses from 100 to 500 kilogray (kGy). The results showed that electromagnetic interference (EMI) shielding effectiveness (SE) was nearly unaltered considering a low content of o-MWCNTs (1 and 5 wt%), however, a slight decrement was noticed for the samples with 20 and 30 wt% addition when the absorbed doses increased from 100 to 500 kGy. In another study[39] coupled semiconductor metal oxide (CSMO) nanocomposites were prepared using a powder metallurgy method, where different concentrations (1, 2.5, and 5%) of CSMO, including Fe_2O_3, TiO_2, and CdO, were individually added to the ZnO–MWCNT composite. Additionally, the gamma-ray shielding ability was designed theoretically, using the MCNPX Monte Carlo code approach for the energies: 0.1, 0.15, 0.2, 0.3, 0.4, 0.5, 0.6, 0.8, and 1 MeV. The data confirmed that increasing energy caused a decrease in the linear attenuation coefficient (μ) value. Nevertheless, the highest linear attenuation coefficient value (and, thus, the lowest half-value layer) was revealed for the composite with 5 wt% addition of CdO for all gamma-ray energies. Interestingly, effects of the ionizing radiation on the properties of composites with the addition of CNTs (or only CNTs[40]) were also studied,[41–43] where it was stated for instance, that the exposure to gamma irradiation did not meaningfully change the value of the glass transition temperature,[41] enhanced the bonding and distribution of nanofillers within the matrix,[42] and caused higher crystallinity of the nanocomposite.[43] Interestingly, considering the

second of the mentioned, one could not forget that a cross-linking reaction could be conducted using gamma radiation, thus eliminating the need to include other chemicals in this process.[44,45]

Despite the above-presented studies on the development of gamma- and X-ray shielding CNT nanocomposites, this field has not gathered adequate attention, indicating a requirement for further comprehensive exploration. This applies to both narrowed down data concerning matrix selection, as well as interest in modifying nanotubes as fillers to achieve superior gamma and X-ray attenuation (*e.g.*, metal encapsulation or MWCNTs surface functionalization with heavy metal compounds). On the other hand, the ease of shaping shields would allow for a customization to various devices, installations, or materials, thereby increasing the effectiveness of protection against the ionizing radiation. Furthermore, it could be perceived, that there is an emerging trend focusing on the development of flexible nanocomposites as this feature undoubtedly positions them as a superior option compared to the conventional solutions.[14,46–49] Such shielding nanocomposites could be tailored to the specific needs and requirements, ensuring the optimal safety measures. It is worth noting that the ability to easily-mold shields paves the way to the more innovative solutions in the field of nuclear energy. Indeed, modern shields could be designed to minimize radiation risks and enhance safety in the nuclear power plants. This, in turn, could contribute to the development of more advanced nuclear technologies that are both energy-efficient and environmentally safe.

The demand for personalized shields seems to be particularly high in the medical sector. Easily formable shields could be tailored to the specific anatomy of each patient, including adjustments for age, figure, and height. This customization would provide optimal protection of the surrounding body parts from harmful radiation exposure and would ensure meeting individual patient needs. Personalized, form-fitting shields could enhance patient comfort by reducing movement restrictions and providing a more secure and personalized experience during diagnostic and therapeutic procedures. Additionally, easily formable shield options have the potential to lower overall costs by avoiding the need for multiple shield productions based on individual patient anatomy, and consequently could reduce waste generated in the medical sector.

In our previous study,[50] as shielding composites against gamma- and X-ray radiation we proposed shape-controlled paraffin-based composites with the addition of iron particles in nano- and microsizes. Iron, as a common and non-toxic element, could be undoubtedly considered as the first-choice filler in the shielding composites; however, CNTs could be considered superior for several reasons. Analyzing their shape and large surface area, the probability of interactions occurring – *e.g.* multiple-scattering interactions due to surface modification of MWCNTs through the presence of heavy elements as discussed by Verma *et al.*[34] thus contributing to the improvement of the shielding property – with incident radiation seems to be greater in comparison to the dispersed individual iron particles. The designed composites should be characterized by stability and durability under the given conditions, thus, one should emphasize that CNTs also exhibit chemical resistance. This characteristic makes them suitable for the more stringent conditions (*e.g.*, with high levels of humidity), where iron particles would undergo corrosion, which could lead to further degradation and weakening of the composite material. Last but not least, the light weight is also a factor considered in the design of shielding composites. Analyzing the density value, CNTs exhibit a lower density compared to iron.

Referring to the aforementioned information, that is on the one hand exploring a non-toxic filler with enhanced shielding capabilities and preserved corrosion resistance, and bearing in mind the scientific focus (concerning radiological protection) on the among others development of flexible shielding nanocomposites, we have manufactured shielding paraffin-based nanocomposites with the addition of Fe@MWCNTs, composed of 9.6 wt% Fe and long MWCNTs (d_{outer} = 54 ± 31 nm, l = 300 μm). Such an Fe-content represents the upper limit of iron phases encapsulation within the nanotube core governed by the maximum solubility of ferrocene in toluene at room temperature (*i.e.* the liquid CVD feedstock). The chosen paraffin, as a chemically neutral matrix, was easily-formable to any shape by the pressure and warmth of hands. Additionally, the studied nanocomposites were simple in terms of composition, *i.e.* only paraffin and Fe@MWCNTs, without the addition of plasticizers or other modifiers. The rationale behind the selection of those ingredients was their low toxicity, in comparison to the traditional lead covers, straightforward processability and recyclability due to the unlimited number of the desired shapes within the range of high performance.

2 Methods and materials

In this section, synthesis and manufacturing protocols toward the Fe@MWCNT-paraffin composites, accompanied by their surface, spectral, and physicochemical characterization with the thereto methods applied, as well as methodology allowing determination of the key final performance, *i.e.*, gamma- and X-ray shielding measurements, are described.

2.1 Synthesis of Fe@MWCNTs

Fe@MWCNTs were synthesized *via* a slightly modified c-CVD protocol, for 16 h[51] with the important change that the feedstock constituted a saturated solution (9.6 wt%) of ferrocene in toluene at 293.15 K. Briefly, catalytic chemical vapor deposition (c-CVD) was employed for producing Fe@MWCNTs. A STF1200 tube furnace (Across International, US) with a single heating zone (1033.15 K) equipped with a syringe pump and a preheater (523.15 K) was applied. The primary carbon source, *i.e.*, toluene, was dosed with 9.6 wt% $FeCp_2$ (catalyst precursor) at a rate of 2.8 mL h^{-1}. The synthetic procedure lasted 24 h at a 1.8 L min^{-1} flow rate of argon as the carrier gas, yielding *ca.* 16 g of Fe@MWCNTs (d_{outer} = 54 ± 31 nm, l = 300 μm) per one synthesis.

2.2 Preparation of Fe@MWCNT–paraffin composites

Paraffin (as a material possessing high hydrogen content) has found utilization as a neutron moderator,[52–54] nevertheless it seems a promising matrix choice for shielding composites (anti gamma and X-rays). Firstly, its properties (*e.g.* melting point[55]) might be different depending on its composition: the length of the hydrocarbon chain and its type (linear or branched chains).[56] It should be noted that paraffin is a cost-effective, commercially approachable (thus confirming the possibility for the composites' production in quantities exceeding lab-scale amounts), and chemically inert compound. In the following study the same batch of paraffin was used as in the previous work.[50] Plastic paraffin was purchased from Orlen Południe Co. Ltd (Trzebinia, Poland). The previously obtained nuclear magnetic resonance (NMR) spectroscopy data[50] allowed for determination of the average n number in the general formula C_nH_{2n+2} to be around 34. However, all summarized paraffin properties including both tabulated data declared by the manufacturer, as well as other experimentally-determined data (Raman spectroscopy, thermogravimetric analysis (TGA), proton nuclear magnetic resonance (^{1}H NMR) and carbon-13 nuclear magnetic resonance (^{13}C NMR) spectra, X-ray diffraction analysis (XRD), and scanning electron microscopy (SEM) pictures) have been published in our previous study.[50]

The Fe@MWCNT–paraffin nanocomposites were manufactured using the cold mixing method. Firstly, the appropriate amount of Fe@MWCNTs and the neat paraffin were weighted on an analytical balance WTC2000 (Radwag, Radom, Poland). Subsequently, the samples were placed in a vacuum dryer Goldbrunn 450 (Berlin, Germany) at 393.15 K, *i.e.*, a temperature above the melting point of paraffin, to remove the residual air. The final step, after the paraffin crystallization, was cold mixing on the previously designed hand press for *ca.* 50 min. Since the shielding properties were measured as a function of the thickness, the composites were placed in 2-cm-high rings. The final samples were prepared at two mass concentrations: 10 and 20 wt% (as a greater Fe@MWCNTs amount would not allow for obtaining the required composite's property – the easy formability provided with the warmth and force of hands), while no plasticizers were used to prepare the nanocomposites. A more detailed description of the manufacturing process (pictures of the manual press, an arrangement of three molds to ensure filling rings in photographs and designs) could be found elsewhere.[50]

2.3 Optical, scanning electron microscopy (SEM), transmission electron microscopy (TEM) images

Optical micrographs were obtained from the transparent and semi-transparent slices using an Octa Microscope under ×5, ×10, and ×20 magnification. The micromorphology of Fe@MWCNTs, paraffin, and their composites was studied by means of a scanning electron microscope (SEM) combined with an EDX SIX HITACHI S-3400 N SEM system analysis (Hemer, Germany). Transmission electron microscopy (TEM) images of Fe@MWCNTs were recorded using a JEOL ARM 200F HRTEM at 200 kV as an accelerating voltage.

2.4 Differential scanning calorimetry (DSC) measurements

Differential scanning calorimetry (DSC) analysis of the neat paraffin and its Fe@MWCNT composites was performed using a Mettler-Toledo DSC 3 calorimeter (operating in the temperature range from 183.15 K to 973.15 K). The samples were sealed in 40 μL standard aluminum crucibles with a single hole punched in the lid. The total mass of the sample was *ca.* 15 mg. Each sample was heated in the temperature range from 258.15 K to 373.15 K. Firstly, the samples were kept at 258.15 K for 5 min, after which the temperature was increased to 373.15 K at a heating rate of 10 K min^{-1}. Then, the samples were cooled to 258.15 K at a rate of −10 K min^{-1} and such a measurement cycle was repeated.

2.5 Thermogravimetric analyses (TGA) measurements

Thermogravimetric analyses (TGA) were acquired from samples placed in a porcelain crucible under both nitrogen and synthetic air (flow rate 10 mL min^{-1}, 5.0 purity) using a TGA8000 thermobalance (PerkinElmer) programmed to a ramp of 25 K min^{-1} from 313.15 K to 1273.15 K.

2.6 Fourier-transform infrared spectroscopy (FTIR) measurements, ultraviolet–visible (UV-Vis) spectroscopy

Fourier-transform infrared spectroscopy (FTIR) was undertaken in a 400–4000 cm^{-1} range. The samples were dried at 383.15 K and ground for 10 min in a porcelain mortar to the concentration of 0.06 wt% with a background subtracted using a pure KBr pellet.

UV-Vis spectra were obtained with a Hitachi U-2910 spectrophotometer from 280 to 1100 nm with 800 nm min^{-1} scan speed. A pure solvent cuvette was placed in the reference channel and a double beam mode was used. Measurements were performed using 10 mm quartz cuvettes. Samples were prepared by submerging paraffin composites (100 mg) in an acetic acid/hydrogen peroxide/sulfuric acid mixture (acetic acid 99.5–99.9% pure p.a. POCH (Poland), hydrogen peroxide solution 30% pure p.a. Chempur (Poland), sulfuric acid 96% pure p.a. Stanlab (Poland)) with a respective volume ratio (5/5/0.1 mL). Composite materials were left in solutions in a glass vial for one month. After this period, 3.5 mL of solution was taken for UV-Vis measurement.

2.7 Rheological measurements

Rheological experiments were conducted using an oscillatory rheometer MCR 302e (Anton Paar, Austria) with a parallel plates system (plate diameter 24.997 mm) and a gap width set to 1.000 mm. The temperature was maintained with a built-in Peltier system with accuracy ±0.01 K. Two types of experiments were conducted to determine viscoelastic properties for pure paraffin and Fe@MWCNT-paraffin composites. First, the amplitude sweep was done with the frequency of oscillations equal to 1 Hz, at temperature 309.75 K. The choice of a 309.75 K temperature was underpinned by the fact that it is the temperature of the human body, and these composites are susceptible to shape change using the warmth and force of bare hands. Then, the temperature sweep was conducted at a set

deformation 0.01% and at a frequency of oscillations of 1 Hz in the temperature range from 288.15 K to 338.15 K with a heating rate of 0.5 K min^{-1}. Data were recorded with a temperature step of 1 K. Based on the calibration procedure, test runs, measurement procedure, sample properties, the expanded uncertainty (coverage factor $k = 2$, confidence level 0.95) of the loss modulus and storage modulus obtained in this work was estimated to be ±3%. All presented results are average of three independent measurements for each type of experiment.

2.8 Gamma shielding measurements

The Fe@MWCNT-paraffin composites were examined in terms of shielding abilities using a ^{60}Co source (activity: 427.5 ± 8.2 kBq, emitted energy: 1.173 and 1.332 MeV, half-life 5.2711 ± 0.0008 years), together with a Geiger–Müller (G–M) counter as a detector (3B Scientific Physics, Hamburg, Germany; dead time: 90 μs). The single measurement included the number of counts collected by the detector for 1 h, while thickness of the samples varied from 0 (number of counts from the ^{60}Co source) to 26 cm with a 2-cm-step. The gamma shielding measurements were repeated three times, and, as the final value the number of counts, N_{exp}, reduced by the experimentally-determined background value, N_{bg}, was taken: $N_{reduced} = N_{exp} - N_{bg}$. The detailed description explaining the selection of one hour as the acquisition time for a single 2-cm-thick layer composite sample together with the picture of the measurement station are given in ref. 50. In order to determine the accuracy of gamma shielding measurements, 100 measurements of the number of counts coming directly from the source ^{60}Co (with an acquisition time of one hour) detected by the G-M counter and 100 measurements of the background value were conducted. The relative uncertainty (the ratio of the standard deviation to the mean value) was estimated based on the detected values directly from the ^{60}Co source that were reduced by the background value. Therefore, the relative uncertainty of the gamma shielding measurements could be estimated as 5%.

2.9 X-ray shielding measurements

In order to determine the X-ray shielding properties of the Fe@MWCNT–paraffin composites, a clinical X-ray diagnostic system, *i.e.*, PROTEUS (which contained a bifocal lamp with X-ray tube focal spot size of 0.6 and 1.2 mm) manufactured by GE Medical Systems, was chosen. The measurements were conducted for various anode voltages, from 70 to 130 kV with a 10-kV-step, and a constant 3.2 mAs the current–time load.

The ''mAs'' designation is a parameter that is the product of the anode current and the exposure duration. It should be remembered, that its increase results in an increase in the patient's dose. The assumed (selected) mAs value could be obtained by changing the ratio of current to exposure time. The design of X-ray machines allows for the regulation of these parameters within a wide range. This is essential when selecting the operating conditions of the X-ray tube for the anatomical region being examined. More importantly, an incorrectly selected ratio of current to exposure time (even with the correct mAs product) might lead to the diagnostic errors. This is particularly important in imaging, *e.g.* the chest, where the minimum possible exposure time and high anode current are required to minimize undesired motion artifacts.

For the data acquisition, a digital detector, produced by AGFA (Mortsel, Belgium), was used. The images, stored in accordance with the DICOM standard, were not subjected to any postprocessing. The calculations utilized numerical values obtained from the detector, which represented the intensity of X-ray radiation that reached the detector after passing through the sample. The digital values within individual fields (neat paraffin, 10 and 20 wt% Fe@MWCNT composites, and without any sample – the aerated field) were read using MATLAB software (produced by The MathWorks, Portola Valley), where the ROI (Region of Interest) field was a square area of 50 × 50 pixels. The X-ray shielding ability was designated as the ratio of the signal intensity obtained from a specific thickness of the sample layer, $I_{layer\ sample}$, to the signal intensity for the aerated field, I_{air}, according to eqn (1) below:

$$\text{X-ray}_{\text{attenuation factor}}{}^{-1} = \frac{I_{\text{layer sample}}}{I_{\text{air}}} = e^{-\mu x}, \qquad (1)$$

where μ is the linear attenuation coefficient (cm^{-1}), and x is the thickness of the material. Based on the conditions of the X-ray measurements, an estimation of the accuracy could be made, indicating a value of ±3%. A more detailed description, along with photos of the measuring station and X-ray tube, is included in ref. 50.

3 Results and discussion

In this section, the results concerning shielding ability (toward both gamma- and X-rays) of the Fe@MWCNT-paraffin composites are summarized. Moreover, the outcomes of rheological measurements, DSC, TGA, FTIR, UV-Vis with imaging analysis (optical micrographs, SEM, TEM) are also presented.

3.1 Imaging analysis: optical micrographs, SEM, TEM

Optical micrographs of paraffin, Fe@MWCNTs, and their composites (Fig. S1, ESI†) showed a partial conservation of the aligned, fibrous-like nature of Fe@MWCNTs in the composites, with different levels of nanotube agglomeration. Further, SEM imaging (Fig. 2) was applied to study the micromorphology of the Fe@MWCNT-paraffin composites, in reference to their neat components. Pristine Fe@MWCNTs were grown as vertically aligned nanotube 'forests', randomly decorated with 'cauliflower'-like C-sp^2 Fe@C spheroids (Fig. 2a). The insets in Fig. 2a show TEM images of individual nanotubes, extracted from the bulk Fe@MWCNT film, which revealed the presence of Fe-based phases (α-Fe, γ-Fe, and Fe_3C)[57] mainly as nanotube-encapsulated, frequently long, fillings, accompanied with Fe@C nanoparticles. Consequently, the herein studied Fe@MWCNTs were found to be more rigid, and more easily breakable than their low-Fe counterparts – here a *ca.* 300-μm-long fragment of a broken Fe@MWCNT carpet was clearly visible.

The wrinkled surface of the neat paraffin (Fig. 2b) and the corresponding composites (Fig. 2c and d) obviously

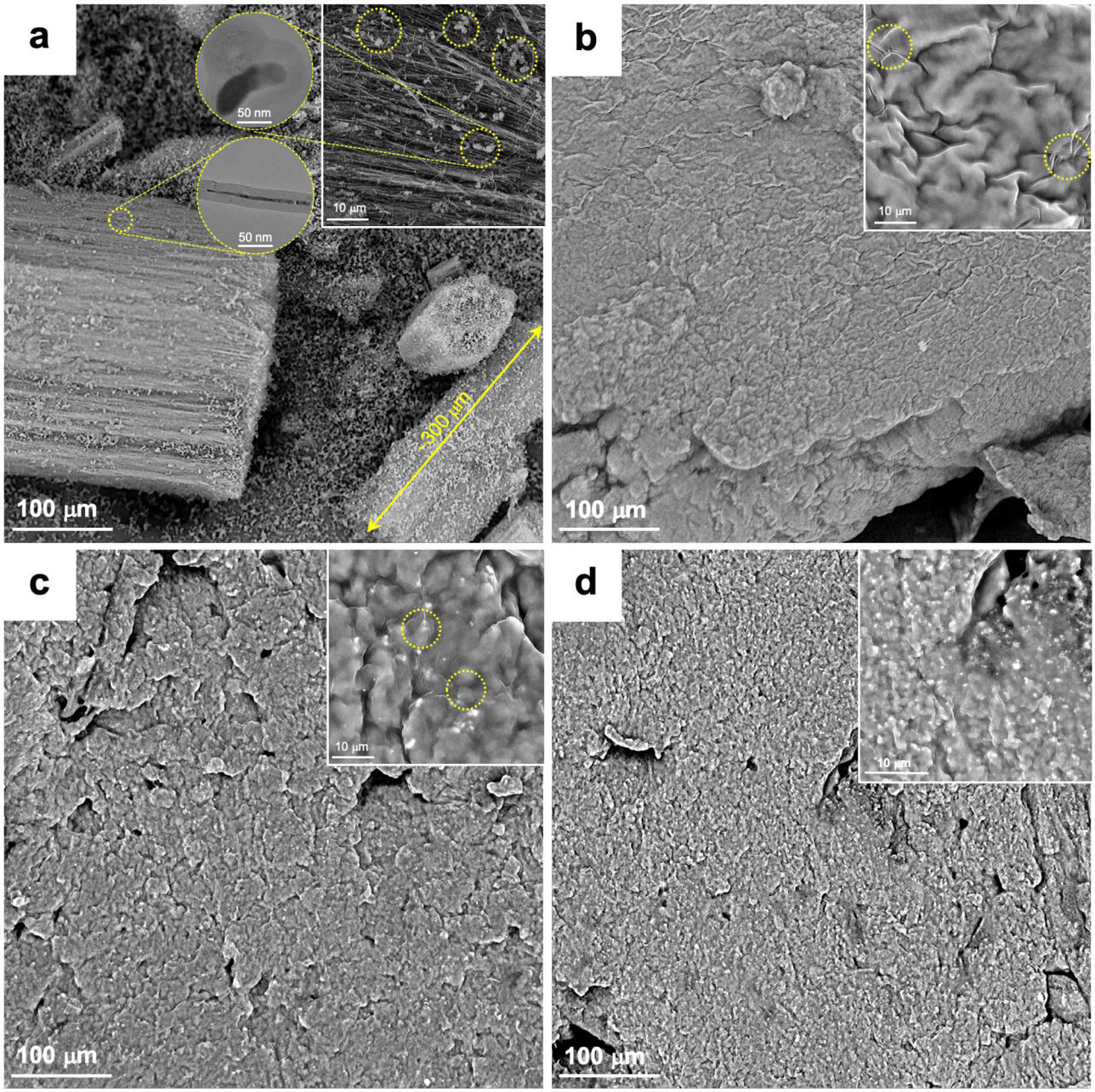

Fig. 2 Scanning electron microscopy (SEM) images, with upper-right insets recorded for higher magnifications, of: as-grown Fe@MWCNTs ['cauliflower'-like spheroidal amorphous Fe@C nanoparticles (circles) and a length of an exemplary broken piece of a rigid Fe@MWCNT 'forest' (double arrow) are highlighted], the left inset shows representative TEM images of Fe@C *versus* Fe@MWCNTs (a); neat paraffin (areas of denser wrinkles highlighted) (b); 10 wt% (c), and 20 wt% (d) Fe@MWCNT–paraffin composites. The circular insets in (a) show TEM images of Fe@MWCNT with the filling *ca.* 400-nm-long and a spheroidal, amorphous-like sp^2-C nanoparticle of Fe@C.

corresponded with their macroscale plasticity (bendability and kneadability), which is important from the perspective of future application in the X- and gamma-ray shields. The Fe@MWCNT content positively correlated with density of the brighter surface spots. Importantly, the Fe-based phases, even for the 20 wt% Fe@MWCNT-based composites, were undetectable by EDX spectroscopy (Fig. S2, ESI†). This outcome confirmed the formation of the paraffin shell on every and each Fe@MWCNT nanoagglomerate in the final composites. The double shell, *i.e.*, nanotube wall and paraffin, emerged as effectively shielding the Fe-core. Importantly from the viewpoint of corrosion resistance and iron (and other possible actively shielding components) leakage, no reaction with the corroding environments, such as 1 M $HCl_{(aq)}$, 1 M $NaCl_{(aq)}$, and 1 M $NaOH_{(aq)}$, also in the presence of the addition of 30 wt% $H_2O_{2(aq)}$ as 1/3 of the final volume of the tested mixture, was detected (Fig. 3). This behavior was opposite to the only-Fe paraffin composites[50] which underwent a progressive digestibility.

Fig. 3 Photograph of a paraffin + 20 wt% Fe@MWCNT composite after a 24 h treatment with 1 M aqueous solutions of NaCl, NaOH, and HCl (from left to right) confirming the composite's durability in the corroding environments.

3.2 DSC and TGA results

The influence of Fe@MWCNTs on the thermal properties of the target composites was studied (Fig. 4 and 5). Firstly, DSC analysis was performed to analyze the possible impact of Fe@MWCNTs on the crystallinity of the paraffin phase (Fig. 4). Neat paraffin and its composites revealed a two-phase crystalline structure with solidification temperatures at *ca.* 309.15 and 327.15 K, with the former one responsible for the warmth-of-hands-derived plasticity of the materials. Clearly, the latent heat of the phase change corroborated the content of the inactive component, *i.e.*, Fe@MWCNTs, in this temperature range. At the same time, the solidification temperature of both composites was found to be higher than for the neat paraffin. This change was indicating possibly a higher level of paraffin crystallinity therein. Indeed, solidification temperatures were found to be 309.25, 309.55, and 309.65 K for the neat paraffin, 10 wt%, and 20 wt% of Fe@MWCNT-paraffin composites, respectively.

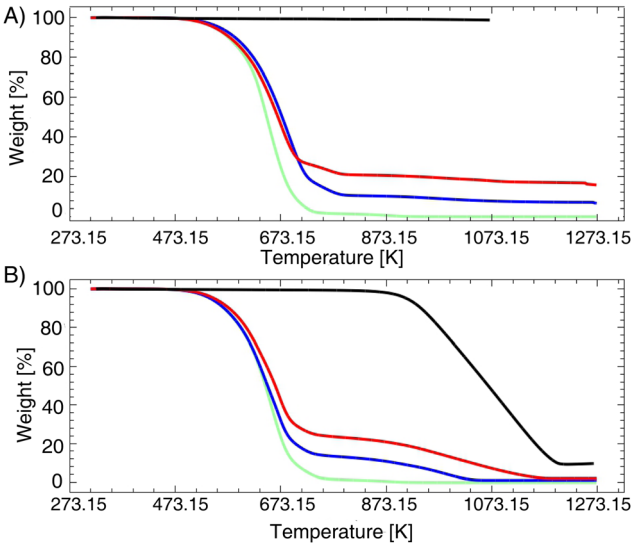

Fig. 5 Thermogravimetric (TGA) curves, recorded under combustional (B) *versus* pyrolytic (N_2) (A) conditions, for the neat paraffin (green), 10 wt% (blue), 20 wt% (red) Fe@MWCNT composites, and pristine Fe@MWCNTs (black).

Strikingly, this tendency was even more pronounced for the other paraffin component – here, solidification temperatures were found to be 326.75, 327.75, and 327.65 K. Based on the literature data, the two crystallization temperatures correspond to *n*-$C_{20}H_{42}$ (*n*-icosane) and *n*-$C_{24}H_{50}$ (*n*-tetracosane) as the main components of the commercial product called 'plastic paraffin'.[58,59] The increase in the crystallization temperature, after removal of the thermal history of the samples, is likely to correlate with the lower

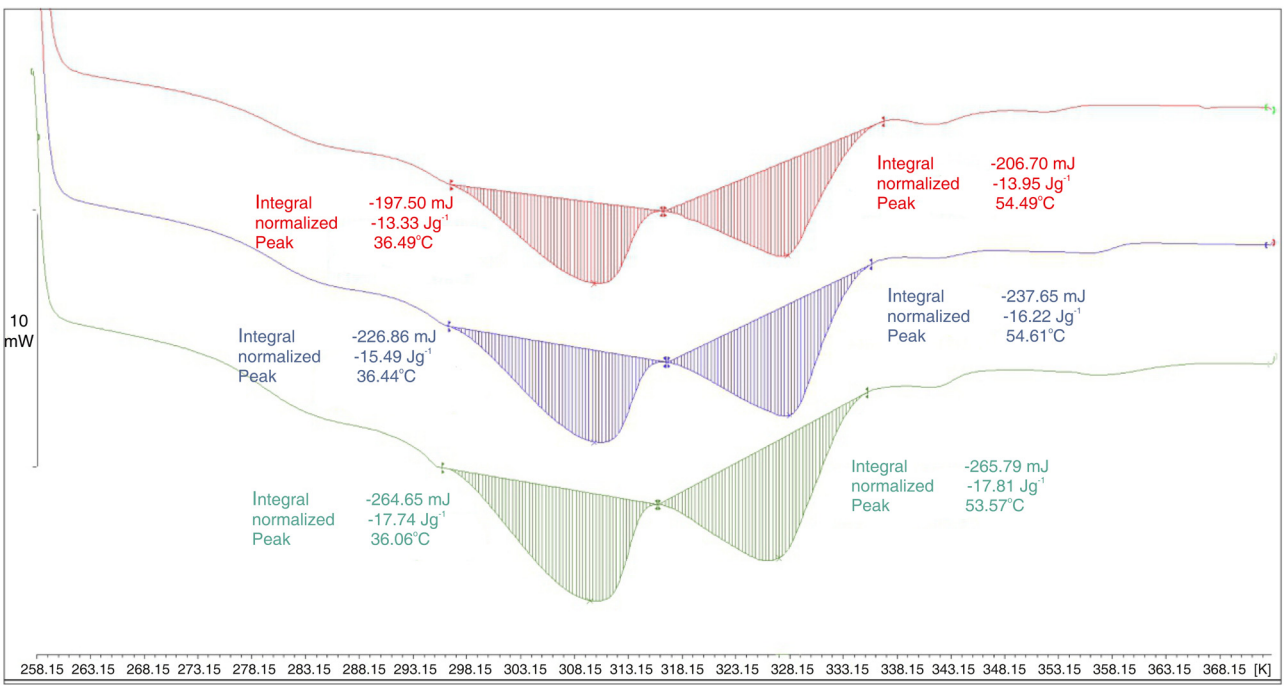

Fig. 4 Differential scanning calorimetry (DSC) curves for neat paraffin (green) and its 10 wt% (blue) and 20 wt% Fe@MWCNT (red) composites.

entropy of the long alkyl chains in the presence of long, dominantly hydrophobic MWCNTs.

At the same time, the decrease in the enthalpy of solidification was found to be practically directly proportional to the Fe@MWCNT content as the latter is a stable-phase solid component: the expected values of the solidification enthalpy for 10 wt% and 20 wt% Fe@MWCNT would be 16.0 and 14.2 J g^{-1} while the actual values were found to be 16.2 and 14.0 J g^{-1}. Further, to study the thermal resistance of Fe@MWCNTs, paraffin, and their composites, TGA – both combustional (Fig. 5B) and pyrolytic (Fig. 5A) – was performed. Pyrolytic TGA, confirming the Fe-content in Fe@MWCNTs, showed that incorporation of Fe@MWCNTs led to an increase in the thermal stability of the composites. This increase in thermal stability under the inert atmosphere would be a result of trapping alkyl and oxygen radicals by Fe@MWCNTs of a higher specific surface area.[60]

3.3 FTIR and UV-Vis results

FTIR analysis (Fig. 6) revealed that all of the key six paraffin modes, practically non-shifted compared to each other, were present in all of the samples (apart from Fe@MWCNTs). This lack of shifts confirmed an ultralow probability of covalent modifications of the nanotubes. Indeed, medium intensity bands at 720 and 730 cm^{-1} could be assigned to $-(CH_2)_n-$ rocking and deforming stretching of C–H, respectively. Further, a weak absorption band at 1378 cm^{-1} could be assigned to symmetric while the strong peak at 1464 cm^{-1} to the asymmetric deformation of methyl groups. In turn, the narrowed bands at 2920 cm^{-1} for the composites – as compared with the broader bands recorded for the neat paraffin – could result from the asymmetric valence CH_2 vibrations in the more crystalline paraffin phase (the symmetric one at 2849 cm^{-1} for CH_3).

In order to employ a paraffin composite filler of the potentially highest shielding efficiency, we have synthesized Fe@MWCNTs using the saturated solution (at 293.15 K) of $FeCp_2$ in toluene (9.6 wt%) as the feedstock. Such an approach led to a total-Fe-encapsulation efficiency at the level of 10 wt% (as previously determined by TGA). Concerning analysis of the micromorphology, optical micrographs of neat paraffin, Fe@MWCNTs,

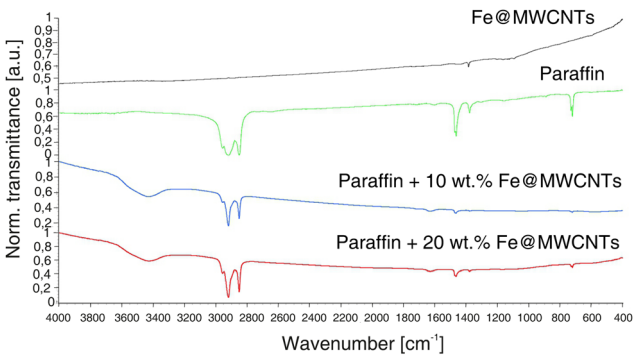

Fig. 6 Fourier-transform infrared (FTIR) spectra of Fe@MWCNTs (black), paraffin (green) and their 10 wt% (blue) and 20 wt% (red) Fe@MWCNT composites.

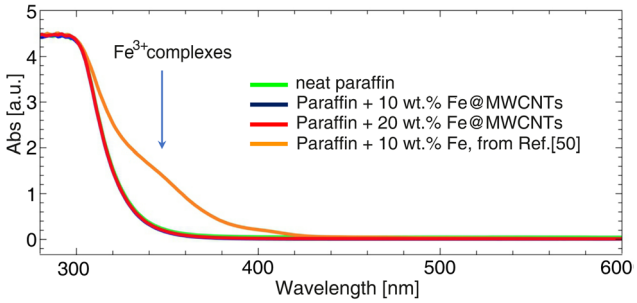

Fig. 7 Ultraviolet–visible light (UV-Vis) spectra of samples treated by a strongly aggressive medium composed from $H_2O_{2(aq)}$ (30%), CH_3COOH (99.5%), and $H_2SO_{4(aq)}$ (96%), (v/v/v = 5 : 5 : 0.1) recorded after one month: neat paraffin (green), 10 wt% Fe@MWCNTs (blue), 20 wt% Fe@MWCNTs (red), Fe–paraffin from ref. 50 (orange).

and their composites (Fig. S1, ESI†) showed a partial conservation of the aligned, fibrous-like nature of Fe@MWCNTs in the composites, with different levels of the nanotube agglomeration. More importantly, samples developed in the previous study[50] as well as the ones with the addition of Fe@MWCNTs were treated with a strongly aggressive medium composed from $H_2O_{2(aq)}$ (30%), CH_3COOH (99.5%), and $H_2SO_{4(aq)}$ (96%), (v/v/v = 5 : 5 : 0.1). The rationale behind this experiment was as follows: if the iron phases would be present exohedrally (anchored to the outer nanotube shell), the immediate reaction of FeOOH (constituting the shell at ambient air temperature) should occur[61] generating Fe^{2+} ions immediately oxidizable to Fe^{3+} ions[62] and further transferred to the strongly acidic bulk digesting solution. While, the UV-Vis spectra developed after one month in the aggressive medium confirmed that samples with the Fe@MWCNTs addition had not experienced a gradual increase in digestibility (Fig. 7). This behavior was opposite to the only-Fe paraffin composites[50] which underwent a progressive digestibility (Fig. 7), thus confirming that composites with Fe@MWCNTs would be more suitable in terms of not releasing into the human organism.

3.4 Rheological properties

The complex rheological behavior of composites containing carbon nanotubes has been well known for over 20 years, and it was described in detail by Du *et al.*[63] They explained that the mechanism of changes in the rheological properties was based on the orientation of nanotubes inside the matrix. Dozens of papers on the experimental studies on viscoelastic properties of nanocomposites containing CNTs can be found in the literature, as was summarized by Chatterjee and Krishnamoorti.[64]

Results of experimental investigation of the rheological properties of Fe@MWCNT-paraffin composites are presented in Fig. 8 and 9. The dependence of the values of the storage (G') and loss (G'') moduli on the deformation at constant temperature 309.75 K are presented in Fig. 8 and listed in Table S1 (ESI†). It could be noted that the developed nanocomposites were stable for low deformations, up to 0.1%, and the critical deformation is higher than that noted for pure paraffin (~0.05%). It has been shown that the proposed nanocomposites could be

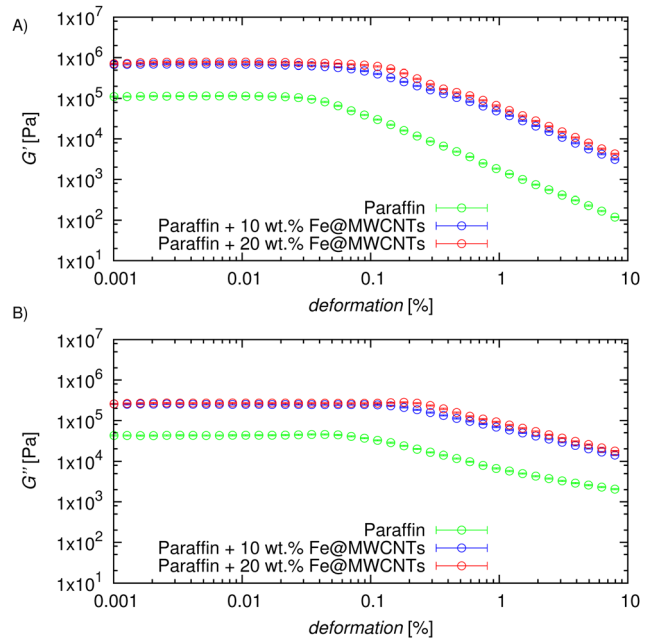

Fig. 8 Storage (G') (A) and loss (G'') (B) moduli as a function of deformation for various mass fractions of nanotubes in nanocomposites at a constant temperature T = 309.75 K and an oscillation frequency of 1 Hz.

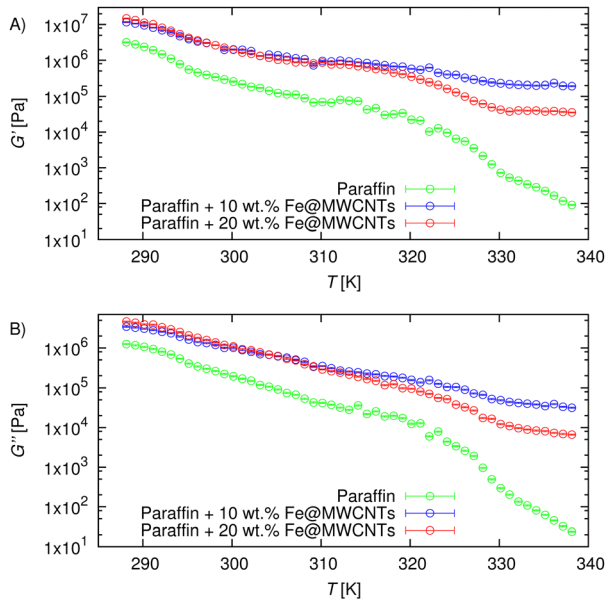

Fig. 9 Storage (G') (A) and loss (G'') (B) moduli as a function of temperature for various mass fractions of nanotubes in nanocomposites at a constant deformation of 0.01% and an oscillation frequency of 1 Hz.

easily formed with bare hands, which is an undoubted improvement over the standard used lead shields.

Findings of the temperature sweep in the temperature range from 288.15 to 338.15 K, at a heating rate of 0.5 K min^{-1}, where the strain was set to 0.01% at frequency equal to 1 Hz are presented in Fig. 9, and summarized in Table S2 (ESI†). As expected, the values of G' and G'' decrease with temperature, however, one could note that in the nanocomposites viscoelastic structure could be consider as stronger.

The rheological experiments included an amplitude sweep at 309.75 K with a frequency equal to 1 Hz, as well as a temperature sweep in the temperature range 288.15 to 338.15 K, at a heating rate of 0.5 K min^{-1}, where the strain was set to 0.01% at a frequency equal to 1 Hz. Tables S1 and S2 (ESI†) contain experimental values of the storage modulus and loss modulus for the pure paraffin as well as Fe@MWCNT-paraffin composites (at various concentrations) for both of the rheological characteristics.

3.5 Gamma shielding properties

One of the parameters determining the ability of a given material to absorb radiation is the linear attenuation coefficient μ (cm^{-1}), which is present in the exponential law of radiation absorption by shields (eqn (2)):

$$N = N_0 e^{-\mu x}, \quad (2)$$

where N and N_0 are the number of counts for the shield and the number of counts coming from the source accordingly, while x is the shield thickness. On the other hand, the more useful quantities are the half-value layer (HVL) and the tenth-value layer (TVL), which represent the thickness of the material that attenuates half of the incident radiation, and the thickness at which the radiation intensity is reduced to 1/10th of its initial value, respectively. The first parameter, half-value layer (HVL), could be defined as (eqn (3)):

$$\mathrm{HVL} = \frac{\ln(2)}{\mu}, \quad (3)$$

where μ is the linear attenuation coefficient (cm^{-1}). Another shielding parameter is the mean free path (MFP), where its calculation provides information about the average distance of a photon between successive collisions:[65,66]

$$\mathrm{MFP} = \frac{1}{\mu}. \quad (4)$$

In this study the linear attenuation coefficient μ (cm^{-1}) was experimentally determined by fitting an exponential curve to the experimental data as the modeled equation (eqn (5)) shows:

$$N_{\mathrm{ratio}} = \frac{N_{\mathrm{reduced\ layer}}}{N_{\mathrm{reduced\ source}}} = e^{-\mu x}, \quad (5)$$

where N_{ratio} is determined by dividing the number of counts for the layer of composite, $N_{\mathrm{reduced\ layer}}$, and number of counts without any layer of composite, $N_{\mathrm{reduced\ source}}$, while μ stands for the linear attenuation coefficient, and x is the thickness of the composite.

In this study, gamma-ray shielding properties of the manufactured composites were determined considering two different Fe@MWCNT mass concentrations. The obtained results are presented in Fig. 10, while the precise data is included in Table S3 (ESI†).

Based on the acquired data it could be noticed, that the addition of Fe@MWCNTs had slightly improved gamma

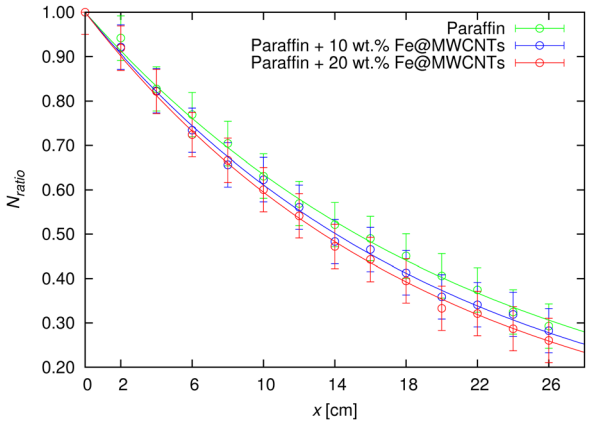

Fig. 10 Ratio of the number of detected photons in the G–M counter for each of the examined layer thicknesses (from 2 to 26 cm with a 2-cm-step) *versus* the number of photons collected without any layer on the paraffin-based composite thicknesses with 10 wt% and 20 wt% addition of Fe@MWCNTs. The symbols and lines represent the experimental and eqn (5) fitting data, respectively.

shielding properties in comparison to the pure paraffin. The summarized linear attenuation coefficients, together with the half value layer data included in Table 1, also demonstrated this relationship.

And so, when analyzing the HVL values, it could be observed that the paraffin thickness of *ca.* 15 cm absorbs half of the incident radiation beam, whereas for the composite with a 20 wt% addition of Fe@MWCNTs *ca.* 13-cm-thickness is required. Fig. 11 presents the bar graph with the HVL values of neat paraffin *versus* its composites, where a decrease in HVL after the addition of nanotubes is visible. The shielding effectiveness, as a result of greater Fe@MWCNTs amount, could be noticed in terms of the MFP (cm) factor (Table 1), where its value decreases analyzing pure paraffin and paraffin + 20 wt% Fe@MWCNTs composite.

It could be observed that the scientific literature discusses the impact of filler concentration on the shielding properties of composites. Therein, a majority of the studies confirmed that a higher content of nano- and micromaterials improved the shielding ability.[67–69] Our studies also confirmed the above data, *i.e.*, μ values for the composites – filled with 10 and 20 wt% of Fe@MWCNTs – were found to be equal to 0.04925 and 0.05195 cm^{-1}, accordingly. Focusing on the μ-values, in comparison to the pure paraffin the linear attenuation coefficient of paraffin + 20 wt% Fe@MWCNTs was ~14% higher, thus confirming that Fe@MWCNTs addition has successfully improved the shielding ability of the matrix. Despite the fact that lead (as the traditional and commonly utilized gamma shield) has superior shielding properties (considering simulation-determined linear attenuation coefficients for lead were $\mu = 0.694 \pm 0.002$ and $\mu = 0.625 \pm 0.002$ cm^{-1} accordingly corresponding to two gamma energies emitted from ^{60}Co: 1773 keV, and 1332 keV[70]) in comparison to the developed paraffin + Fe@MWCNTs composites, it should be emphasized that the latter could be characterized as a non-toxic shield option with versatility in shape definition provided simply with the warmth and force of hands – features that cannot be attributed to the strictly-determined shapes of Pb-based covers.

Focusing on the shielding mechanism, the photoelectric effect, Compton scattering and electron positron pair production should be named as the three mainly occurring phenomena in the case of gamma rays interaction with matter – the γ-ray energy (MeV) and the atomic number of the material (Z) determine which effect dominates.[71] In the current study, considering the used fillers (Fe@MWCNTs) along with the utilized source (^{60}Co, ~1 MeV energy), the Compton effect – inelastic scattering of the incident beam on electrons (whose binding energy is much smaller than the energy of the incident radiation beam), where as a result of this phenomenon the electron is ejected and the remaining photon with a lower energy changes the direction of its propagation (in accordance with the principle of conservation of energy and momentum) – seems to be the most probable for the shielding mechanism.[72,73]

3.6 X-ray shielding properties

The X-ray shielding ability of the Fe@MWCNT-paraffin composites was experimentally evaluated for two different filler contents across a wide range of anode voltages (70 to 130 kV with 10 kV increments). However, the following analysis focused only on the 70 kV voltage value. The choice of 70 kV voltage was dictated by the fact, that this value is often used in the range of X-ray diagnostics. The selection of voltage in medical imaging is influenced by both the area being examined in terms of anatomical region and the posture of the patient. It should be also noted that X-ray machines allow for adjusting the anode voltage with a resolution of 1 kV. This feature was crucial in imaging using X-ray medical films, where the highly non-linear characteristic required voltage adjustment with high resolution. Nowadays, in the era of digital detectors with linear processing characteristics, the resolution of setting the voltage on the X-ray tube has less practical significance. Nonetheless, the outcomes for other values of anode voltage are presented

Table 1 Summary of the experimentally determined linear attenuation coefficients, μ (cm^{-1}), accompanied by uncertainty, half value layer, HVL (cm) with calculated uncertainty (coverage factor $k = 2$), and mean free path, MFP (cm) with calculated uncertainty (coverage factor $k = 2$) for all of the studied samples

Sample	μ (cm^{-1})	HVL (cm)	MFP (cm)
Paraffin	0.04550 ± 0.00047	15.23 ± 0.31	21.98 ± 0.45
Paraffin + 10 wt% Fe@MWCNTs	0.04925 ± 0.00050	14.07 ± 0.29	20.30 ± 0.41
Paraffin + 20 wt% Fe@MWCNTs	0.05195 ± 0.00044	13.34 ± 0.23	19.25 ± 0.33

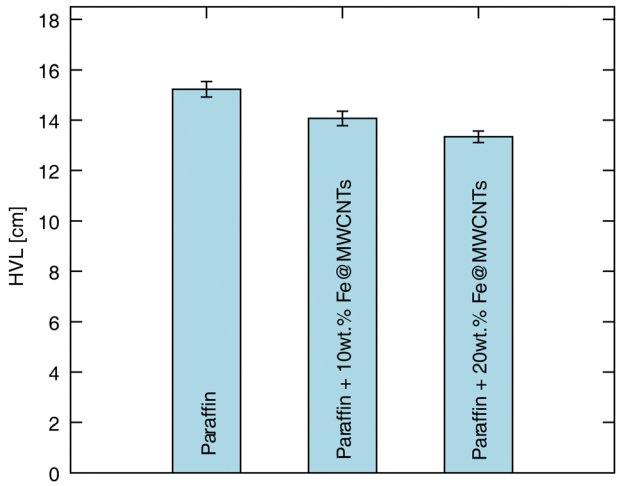

Fig. 11 Half value layer (HVL) of the manufactured Fe@MWCNT–paraffin composites, and pure paraffin presented in the single bars confirming the HVL value decrease with higher Fe@MWCNTs content. Table 1 provides the specific HVL values, along with their corresponding uncertainties.

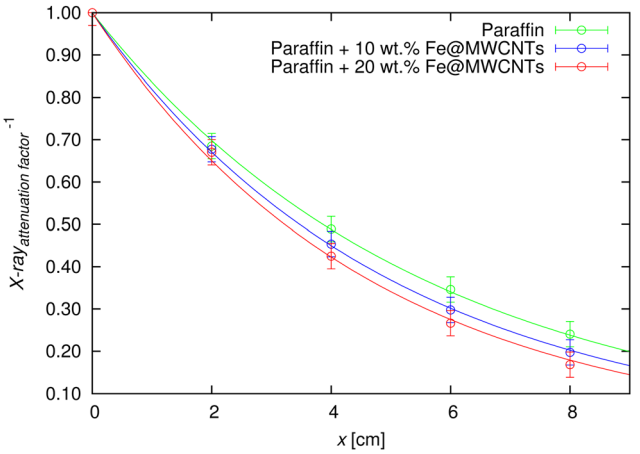

Fig. 12 Dependence of the X-ray$_{\text{attenuation factor}}^{-1}$ for different thicknesses (2, 4, 6, and 8 cm) for the pure paraffin and paraffin-based composites with 10 wt% and 20 wt% addition of Fe@MWCNTs at the 70 kV anode voltage. The symbols present the experimentally-achieved data, while the lines present the eqn (7) fitting data.

also in Fig. S3 (ESI†), while the specific values are summarized in Tables S4–S10 in the ESI.†

The basic law that presents the attenuation of incident X-rays after interaction with shields could be formulated as:

$$\frac{I}{I_0} = e^{-\mu x}, \tag{6}$$

where I is the signal intensity after passing through the shield, I_0 is the signal intensity without shield, μ is the linear attenuation coefficient (expressed in cm^{-1}), and x is the shield thickness.

The linear attenuation coefficient determined for the Fe@MWCNT–paraffin composites, and neat paraffin, was established by a fitting modeled equation to the experimentally-obtained data:

$$\text{X-ray}_{\text{attenuation factor}}^{-1} = \frac{I_{\text{layer sample}}}{I_{\text{air}}} = e^{-\mu x}, \tag{7}$$

where $I_{\text{layer sample}}$ is the signal intensity from the applied thickness of the composite sample, I_{air} is the signal intensity without any composite sample, μ is the linear attenuation coefficient, and x is the thickness of the composite sample.

The experimental data, together with the fitted curves (eqn (7)), are depicted in Fig. 12, while the μ values for paraffin, nanotube composites (along with calculated HVL, MFP values) are summarized in Table 2.

It could be stated that the increasing Fe@MWCNT content contributed to the X-ray shielding ability improvement: the HVL-values of the neat paraffin and 20 wt% Fe@MWCNTs were 3.861 and 3.220 cm, respectively. The superior X-ray attenuation could be noticed in composites with greater Fe@MWCNTs amount in terms of MFP factor, as the lower MFP value confirms improved shielding properties. Again, the literature reports a similar trend, where greater filler amount influenced the MFP value decrement.[74–76]

4 Conclusions

Nano- and microcomposites constitute an important alternative to the traditional shields used against ionizing radiation. Selecting the most prospective components (including those at the nanosize, main components, and other additives such as plasticizers, modifiers, *etc.*) and technological process enables the shield design for the targeted applications.

Here, we have designed, developed and elaborated shielding composites based on paraffin with the addition of Fe@MWCNTs (at concentrations of 10 and 20 wt%), which were tested for their shielding abilities against gamma- and X-ray radiation. The developed composites were characterized by their simplicity of composition (where only two components were utilized), with a commonly available, ready-to-use, chemically inert and inexpensive matrix. The Fe@MWCNT filler allowed for the development of a non-toxic composite (Pb-free), and its addition has successfully enhanced the shielding properties of paraffin due to the

Table 2 Summary of experimentally-determined linear attenuation coefficient, μ (cm^{-1}), with uncertainty, determined half value layer, HVL (cm) with calculated uncertainty (coverage factor k = 2), and mean free path, MFP (cm) with calculated uncertainty (coverage factor k = 2) for paraffin and composites filled with 10 and 20 wt% Fe@MWCNTs at the 70 kV anode voltage

Sample	μ (cm^{-1})	HVL (cm)	MFP (cm)
Paraffin	0.1795 ± 0.0020	3.861 ± 0.086	5.571 ± 0.124
Paraffin + 10 wt% Fe@MWCNTs	0.1997 ± 0.0016	3.470 ± 0.056	5.008 ± 0.080
Paraffin + 20 wt% Fe@MWCNTs	0.2152 ± 0.0040	3.220 ± 0.120	4.647 ± 0.173

combination of MWCNTs with an encapsulated metal (Fe) compound inside. The conducted research confirmed the dependence of the shielding capability on the amount of the added Fe-encapsulated nanotube filler. More importantly, as the outcome of the studies on the behavior of the paraffin + 20 wt% Fe@MWCNT nanocomposites under harsh, corroding conditions presents the individual ingredients will not be released into the human body and the environment. It should be also noted that the final composites featured a simple processing (without any need for highly specialized equipment), and minimalism in terms of composition. This leads to a reduction in the production time and cost, energy savings, and, more importantly, availability to a broad spectrum of researchers, industry and medical workers, and material engineering designers (especially including radiological protection). Although the proposed nanocomposites have a weaker ability to attenuate radiation than pure lead, due to their advantages such as low density, non-toxicity and ease of formation, they could be an alternative to these classic radiation protection materials. Summing up, it has been shown that the use of nanotubes significantly reduces susceptibility to corrosion and increases the stability of nanocomposites, which is crucial keeping in mind durability and the multi-aspect nature of the working conditions.

Bearing in mind the susceptibility of Fe@MWCNT-paraffin composites in terms of shape definition at average room temperature under pressure and heat from the hand touch it should be stated that such a solution overcomes a challenge where manufacturing complex traditional covers is impossible or shape changes could not be developed to a satisfactory degree (thus requiring the repetition of the manufacturing procedure). The developed Fe@MWCNT-paraffin composites could be implemented in various areas of our every-day life research and scientific facilities, *i.e.*, as: (1) a supportive element in the shielding constructions, (2) adjusted containers for radioactive waste transport, (3) personalized shields for patients in hospitals (*e.g.*, to protect sensitive areas of the body during X-ray imaging), (4) for workers exposed to ionizing radiation (*e.g.* in the nuclear energy sector), and (5) to shield, and maintain undisturbed working of sensitive electronic equipment placed in areas of radiation exposure.

This study identifies a few gaps; therefore, the following potential future directions are outlined. Firstly, development of the composites, including CNTs, could be recognized as remaining in the early stages of progress (as they have not received wide attention as in the case of heavy particles[1]), the research should be continued with insight into the X and gamma-ray attenuating properties of nanotubes varying in morphology. This includes combinations of the number of walls (SW- or MWCNTs), the potential influence of the concentration of the encapsulated compound (if any) inside the carbon nanotubes, and the presence of periodically distributed heavy metal compounds on the nanotube surface (including pure nanoparticles such as Pb, W, Bi, *etc.*, as well as their compounds/oxides), among other factors. As alternatives, since MWCNTs could be synthesized *via* c-CVD from various (non-)metallic precursors,[77–81] other nanoparticle@MWCNT systems could be used as equally or even more promising fillers. Comparative shielding tests between commercial CNT products and those laboratory-synthesized should not be omitted. The various orientations of carbon nanotubes (again, considering variety of CNTs morphology) should be analyzed more comprehensively to understand their impact on the shielding properties of the developed composites.[82] Maintaining versatility in matrix selection is also crucial as it not only provides a comprehensive overview of real-world shielding nanocomposites implementation possibilities but also facilitates the creation of databases essential for developing theoretical models. Considering the unique mechanical properties of carbon nanotubes along with variety in terms of matrix selection it is essential to not only determine the shielding properties (X, gamma), but also to evaluate the rheological properties of the developed shielding composites. Moreover, other studies should be added reflecting the durability aspect (the effect of gamma or X-rays on the composite in terms of damage), and the examination of gamma-ray shielding properties should be included over a broader energy range (using other sources). Finally, as carbon nanotubes are recognized for EMI shielding and microwave absorption,[83,84] while paraffin is for neutron shielding, the developed hybrid paraffin + Fe@MWCNTs composites could be examined in these two areas to verify additional (diverse) attributes.

Author contributions

Conceptualization: A. T., S. B. and G. Ż.; data curation: J. S. and A. T.; formal analysis: J. S., A. T. and G. Ż.; funding acquisition: M. D. and S. B.; investigation: J. S., A. T., K. C., S. R., A. K., R. G. J., S. W., M. D., S. B. and G. Ż.; methodology: J. S., A. T. and G. Ż.; project administration: M. D., S. B. and G. Ż.; resources: M. D., S. B. and G. Ż.; software: J. S. and A. T.; supervision: M. D., S. B. and G. Ż.; visualization: J. S., A. T., S. R., S. W., M. D., S. B. and G. Ż.; writing – original draft: J. S., A. T., S. R., S. W., S. B. and G. Ż.; writing – review & editing: M. D., S. B. and G. Ż.

Data availability

The data supporting this article have been included as part of the ESI.†

Conflicts of interest

There are no conflicts to declare.

Acknowledgements

The authors acknowledge the supporting actions from the EU's Horizon 2020 ERA-Chair project ExCEED, grant agreement No. 952008. S. R., R. G. J., A. K., and S. B. are very grateful for the financial support from the National Science Centre (Poland), Grant No. 2019/33/B/ST5/01412 in the framework of the OPUS

program. K. C. and M. D. are very grateful for the financial support from the National Science Centre (Poland), Grant No. 2021/41/B/ST5/00892 in the framework of the OPUS program.

Notes and references

1 J. Sobczak and G. Żyła, *Energy*, 2024, **290**, 130210.
2 P. Sowa, J. Rutkowska-Talipska, U. Sulkowska, K. Rutkowski and R. Rutkowski, *Polish Ann. Med.*, 2012, **19**, 134–138.
3 F. H. Fahey, A. Goodkind, S. T. Treves and F. D. Grant, *J. Radiol. Nursing*, 2016, **35**, 5–11.
4 J. Epp, *Materials characterization using nondestructive evaluation (NDE) methods*, Elsevier, 2016, pp. 81–124.
5 M. Scimeca, S. Bischetti, H. K. Lamsira, R. Bonfiglio and E. Bonanno, *Eur. J. Histochem.*, 2018, **62**, 89–98.
6 T. A. Harroun, N. Kučerka, M.-P. Nieh and J. Katsaras, *Soft Matter*, 2009, **5**, 2694–2703.
7 M. Pricaz and A.-C. Uță, *Rom. J. Biophys.*, 2015, **25**, 143–162.
8 S. Kumar and D. Mahto, *Int. J. Sci. Eng. Res.*, 2013, **4**, 183–195.
9 S. Sadekin, S. Zaman, M. Mahfuz and R. Sarkar, *Energy Proc.*, 2019, **160**, 513–518.
10 A. Ara and J. A. Usmani, *et al.*, *Interdiscip. Toxicol.*, 2015, **8**, 55–64.
11 N. J. AbuAlRoos, N. A. B. Amin and R. Zainon, *Radiat. Phys. Chem.*, 2019, **165**, 108439.
12 S. Mortazavi, J. J. Bevelacqua, P. Rafiepour, S. Sina, J. Moradgholi, A. Mortazavi and J. S. Welsh, *Advanced Radiation Shielding Materials*, Elsevier, 2024, pp. 305–322.
13 E. Mansouri, A. Mesbahi, R. Malekzadeh and A. Mansouri, *Radiat. Environ. Biophys.*, 2020, **59**, 583–600.
14 Q. Li, R. Zhong, X. Xiao, J. Liao, X. Liao and B. Shi, *ACS Appl. Mater. Interfaces*, 2020, **12**, 54117–54126.
15 H. O. Tekin, V. P. Singh and T. Manici, *Appl. Radiat. Isot.*, 2017, **121**, 122–125.
16 H. M. Zakaly, G. ALMisned, S. A. Issa, V. Ivanov and H. O. Tekin, *J. Aust. Ceram. Soc.*, 2023, **59**, 127–135.
17 Ö. Başgöz, S. H. Güler, Ö. Güler, C. A. Canbay, H. M. Zakaly, S. A. Issa, G. ALMisned and H. O. Tekin, *Diamond Relat. Mater.*, 2022, **126**, 109095.
18 M. E. Mahmoud, A. M. El-Khatib, M. S. Badawi, A. R. Rashad, R. M. El-Sharkawy and A. A. Thabet, *J. Cleaner Prod.*, 2018, **176**, 276–287.
19 R. M. El-Sharkawy, F. S. Abdou, M. Gizawy, E. A. Allam and M. E. Mahmoud, *Radiat. Phys. Chem.*, 2023, **208**, 110838.
20 A. M. El-Khatib, Y. M. Abbas, M. S. Badawi, O. M. Hagag and M. T. Alabsy, *Phys. Scr.*, 2021, **96**, 125316.
21 M. E. Mahmoud, R. M. El-Sharkawy, E. A. Allam, R. Elsaman and A. El-Taher, *J. Alloys Compd.*, 2019, **803**, 768–777.
22 S. Jayakumar, T. Saravanan and J. Philip, *Hybrid Adv.*, 2023, **4**, 100100.
23 A. H. Alsaab and S. Zeghib, *Polymers*, 2023, **15**, 2142.
24 A. Kolanowska, D. Janas, A. P. Herman, R. G. Jędrysiak, T. Giżewski and S. Boncel, *Carbon*, 2018, **126**, 31–52.
25 J. Hu, Y. Hu, Y. Ye and R. Shen, *Chem. Eng. J.*, 2023, **452**, 139147.
26 X. Zhang, C. Deng, R. Xu and D. Wang, *J. Mater. Sci.*, 2007, **42**, 8377–8380.
27 M. Zhang and J. Li, *Mater. Today*, 2009, **12**, 12–18.
28 Z. Ali, S. Yaqoob, J. Yu and A. D'Amore, *Compos., Part C: Open Access*, 2024, **13**, 100434.
29 N. Mohd Nurazzi, M. M. Asyraf, A. Khalina, N. Abdullah, F. A. Sabaruddin, S. H. Kamarudin, S. Ahmad, A. M. Mahat, C. L. Lee and H. Aisyah, *et al.*, *Polymers*, 2021, **13**, 1047.
30 S. Verma, B. Sarma, K. Chaturvedi, D. Malvi and A. K. Srivastava, *Compos. Interfaces*, 2023, **30**, 223–251.
31 R. Kumar, S. Sahoo, E. Joanni, R. K. Singh, W. K. Tan, K. K. Kar and A. Matsuda, *Carbon*, 2021, **177**, 304–331.
32 H. Xu, S. M. Anlage, L. Hu and G. Gruner, *Appl. Phys. Lett.*, 2007, **90**, 183119.
33 A. Katheria, P. Das, J. Nayak, K. Nath, S. K. Ghosh, S. Paul and N. C. Das, *J. Phys. Chem. Solids*, 2023, **179**, 111395.
34 S. Verma, M. Mili, C. Sharma, H. Bajpai, K. Pal, D. Qureshi, S. Hashmi and A. Srivastava, *Green Chem. Lett. Rev.*, 2021, **14**, 272–285.
35 T. Fujimori, S. Tsuruoka, B. Fugetsu, S. Maruyama, A. Tanioka, M. Terrones, M. S. Dresselhaus, M. Endo and K. Kaneko, *Mater. Express*, 2011, **1**, 273–278.
36 M. Altarawneh, M. Aladailaha and O. Al-Madanat, *East Eur. J. Phys.*, 2023, 524–530.
37 W. Zhang, H. Xiong, S. Wang, M. Li, Y. Gu and R. Li, *Mater. Express*, 2016, **6**, 456–460.
38 F. Huang, Y. Wang, P. Wang, H.-L. Ma, X. Chen, K. Cao, Y. Pei, J. Peng, J. Li and M. Zhai, *RSC Adv.*, 2018, **8**, 24236–24242.
39 O. Basgoz, O. Guler, E. Evin, C. Yavuz, G. ALMisned, S. A. Issa, H. M. Zakaly and H. O. Tekin, *Ceram. Int.*, 2022, **48**, 16251–16262.
40 B. Safibonab, A. Reyhani, A. N. Golikand, S. Mortazavi, S. Mirershadi and M. Ghoranneviss, *Appl. Surf. Sci.*, 2011, **258**, 766–773.
41 P. O. Muisener, L. Clayton, J. D'Angelo, J. Harmon, A. Sikder, A. Kumar, A. Cassell and M. Meyyappan, *J. Mater. Res.*, 2002, **17**, 2507–2513.
42 A. T. Mou'ad, S. A. Saraireh, R. S. Chen, S. H. Ahmad, M. A. Al-Tarawni and L. J. Yu, *Radiat. Phys. Chem.*, 2021, **179**, 109168.
43 M. Martínez-Morlanes, P. Castell, V. Martínez-Nogués, M. Martinez, P. J. Alonso and J. Puértolas, *Compos. Sci. Technol.*, 2011, **71**, 282–288.
44 L. Bonetti, L. De Nardo and S. Farè, *Soft Matter*, 2023, **19**, 7869–7884.
45 M. S. T. and T. Mondal, *Soft Matter*, 2021, **17**, 6284–6297.
46 S. Wu, J. Bao, Y. Gao, W. Hu and Z. Lu, *J. Mater. Sci.*, 2024, **59**, 8109–8133.
47 S. M. Kassem, M. A. Maksoud, M. M. Ghobashy, A. M. El Sayed, S. Ebraheem, A. Helal and Y. Ebaid, *Radiat. Phys. Chem.*, 2023, **209**, 110953.
48 M. Irfan, M. Aslam and Z. A. Raza, *Polym. Bull.*, 2023, **80**, 791–807.
49 M. Khalifa, A. M. El Sayed, S. M. Kassem and E. Tarek, *Sci. Rep.*, 2024, **14**, 3672.

50 J. Sobczak, A. Truszkiewicz, E. Korczeniewski, A. Cyganiuk, A. P. Terzyk, A. Kolanowska, R. G. Jędrysiak, S. Boncel and G. Żyła, *ACS Appl. Eng. Mater.*, 2023, **1**, 3237–3253.
51 S. Boncel, A. P. Herman, S. Budniok, R. G. Jędrysiak, A. Jakóbik-Kolon, J. N. Skepper and K. H. Müller, *ACS Biomater. Sci. Eng.*, 2016, **2**, 1273–1285.
52 D. Toyen and K. Saenboonruang, *J. Nucl. Sci. Technol.*, 2017, **54**, 871–877.
53 Y. Zhang, F. Chen, X. Tang, H. Huang, M. Ni and T. Chen, *J. Compos. Mater.*, 2018, **52**, 953–962.
54 A. H. M. Fahmi, M. A. Sazali, K. Yazid, A. A. A. Bakar, N. S. M. Ali, K. Jamaluddin and M. S. Sarkawi, *Radiat. Phys. Chem.*, 2024, **218**, 111639.
55 P. Flory and A. Vrij, *J. Am. Chem. Soc.*, 1963, **85**, 3548–3553.
56 A. Palou, J. Cruz, M. Blanco, R. Larraz, J. Frontela, C. M. Bengoechea, J. M. González and M. Alcalá, *Energy Fuels*, 2014, **28**, 956–963.
57 S. Boncel, A. Pluta, M. Skonieczna, A. Gondela, B. Maciejewska, A. P. Herman, R. G. Jędrysiak, S. Budniok, K. Komędera and A. Błachowski, *et al.*, *J. Nanomater.*, 2017, **2017**, 1262309.
58 V. Kuryakov and D. Ivanova, *J. Phys.: Conf. Ser.*, 2019, **1385**, 012045.
59 P. A. Levene and C. J. West, *J. Biol. Chem.*, 1916, **26**, 115–120.
60 K. K. Koziol, S. Boncel, M. S. Shaffer and A. H. Windle, *Compos. Sci. Technol.*, 2011, **71**, 1606–1611.
61 S.-S. Lin and M. D. Gurol, *Environ. Sci. Technol.*, 1998, **32**, 1417–1423.
62 W. Koppenol, *Free Radical Biol. Med.*, 1993, **15**, 645–651.
63 F. Du, R. C. Scogna, W. Zhou, S. Brand, J. E. Fischer and K. I. Winey, *Macromolecules*, 2004, **37**, 9048–9055.
64 T. Chatterjee and R. Krishnamoorti, *Soft Matter*, 2013, **9**, 9515–9529.
65 H. Manjunatha, *Radiat. Phys. Chem.*, 2017, **137**, 254–259.
66 A. H. Almuqrin, M. Rashad, C. V. More, M. Sayyed and M. Elsafi, *Radiat. Phys. Chem.*, 2024, **222**, 111824.
67 M. T. Alabsy, M. I. Abbas, A. Y. El-Khatib and A. M. El-Khatib, *Sci. Rep.*, 2024, **14**, 1279.
68 N. Plangpleng, P. Charoenphun, D. Polpanich, K. Sakulkaew, N. Buasuwan, O. Onjun and K. Chuamsaamarkkee, *Radiat. Phys. Chem.*, 2022, **199**, 110311.
69 S. Yazdani-Darki, M. Eslami-Kalantari, S. Feizi and H. Zare, *Radiat. Phys. Chem.*, 2023, **209**, 110966.
70 S. Shirmardi, M. Shamsaei and M. Naserpour, *Ann. Nucl. Energy*, 2013, **55**, 288–291.
71 G. R. Choppin, J.-O. Liljenzin and J. Rydberg, *Radiochem. Nucl. Chem.*, 2002, 123–165.
72 C. Davidsson, in *Alpha-, Beta- and Gamma-Ray Spectroscopy*, ed. K. Siegbahn, Elsevier, 1968, pp. 37–78.
73 B. Li, Y. Feng, K. Ding, G. Qian, X. Zhang and J. Zhang, *Carbon*, 2013, **60**, 186–192.
74 D. Erwina, H. Heryanto and D. Tahir, *Radiat. Phys. Chem.*, 2023, **210**, 111053.
75 S. F. Alanazi, N. M. Alotaibi, M. Alsuhybani, N. Alnassar, F. I. Almasoud and M. Almurayshid, *Polymers*, 2024, **16**, 1212.
76 M. S. Gharissah, A. Ardiansyah, S. R. Pauziah, N. A. Muhammad, R. Rahmat, H. Heryanto and D. Tahir, *Sci. Rep.*, 2022, **12**, 19169.
77 B. Zheng, C. Lu, G. Gu, A. Makarovski, G. Finkelstein and J. Liu, *Nano Lett.*, 2002, **2**, 895–898.
78 R. Fernández-Loyola, M. Muthuvel, A. Hernández-Maldonado, J. Menchaca-Rivera, J. Perez-Robles, O. Solorza-Feria and G. Botte, *Ceram. Int.*, 2021, **47**, 13604–13612.
79 Y. Hayashi, T. Fujita, T. Tokunaga, K. Kaneko, T. Butler, N. Rupesinghe, J. Carey, S. Silva and G. Amaratunga, *Diamond Relat. Mater.*, 2007, **16**, 1200–1203.
80 Y. Zhang, W. Zhou, Z. Jin, L. Ding, Z. Zhang, X. Liang and Y. Li, *Chem. Mater.*, 2008, **20**, 7521–7525.
81 R. Ummethala, D. Wenger, S. F. Tedde, C. Täschner, A. Leonhardt, B. Büchner and J. Eckert, *J. Appl. Phys.*, 2016, **119**, 044302.
82 M. Al-Mamun, J. Chen, M. Burda and K. K. Koziol, *Mater. Chem. Phys.*, 2023, **309**, 128318.
83 X. Liu, X. Yin, L. Kong, Q. Li, Y. Liu, W. Duan, L. Zhang and L. Cheng, *Carbon*, 2014, **68**, 501–510.
84 N. Li, Y. Huang, F. Du, X. He, X. Lin, H. Gao, Y. Ma, F. Li, Y. Chen and P. C. Eklund, *Nano Lett.*, 2006, **6**, 1141–1145.